# Correlation Symmetry Analysis of Electron Nanodiffraction from Amorphous Materials

Shuoyuan Huang <sup>a</sup>, Carter Francis <sup>a</sup>, Jittisa Ketkaew <sup>b</sup>, Jan Schroers <sup>b</sup>, Paul M. Voyles <sup>a</sup>, \*

- <sup>a</sup> Department of Materials Science and Engineering, University of Wisconsin Madison, Madison, Wisconsin 53706, USA
- <sup>b</sup> Mechanical Engineering, Yale University, New Haven, Connecticut 06511, USA
- \* paul.voyles@wisc.edu

Abstract Angular symmetry in nanodiffraction reflects rotational symmetry in the sample. We introduce the angular symmetry coefficient as a method to extract local symmetry information from electron nanodiffraction patterns of amorphous materials. Symmetry coefficients are the average of the angular autocorrelation function at the characteristic angles of a particular rotational symmetry. The symmetry coefficients avoid artifacts arising from Fourier transformation and Friedel symmetry breakdown that affect the angular power spectrum approach to determining angular symmetries in amorphous nanodiffraction. Both methods require thin samples to avoid overlapping diffraction from clusters of atoms separated in the thickness of the sample, but symmetry coefficients are more forgiving. Electron nanodiffraction experiments on a Pd-based metallic glass sample demonstrate both potentially misleading information in angular power spectrum and the utility of symmetry coefficients.

**Keywords:** Electron nanodiffraction; Rotational symmetry; Correlation symmetry analysis; Amorphous structure

# 1. Introduction

To understand some of their exceptional properties and to gain insight into glass formation, we need to study the structure of glasses [1–3]. However, structural characterization of glasses remains a major challenge. The lack of long-range periodicity makes an analytical description of the positions of all atoms in a glass structure impossible, short of simply listing them. As a result, descriptions of glass structure have tended to emphasize simple rules such as dense packing [4], preservation of coordination numbers and bond angles [5], or statistical or topological abstractions of atomic configurations [6] (*i.e.* Frank-Kasper polyhedra [7,8], topological rings/clusters of bonds [9], or indices describing Voronoi polyhedra [10]). In metallic glasses, approximate rotational symmetry has been identified as a potential important feature of local structure. Many metallic glasses are reported to have a structure with some icosahedral local ordering [11], which is characterized by distinct 5-fold rotation symmetry. 5-fold symmetry is incompatible with crystalline translation symmetry, so is thought to favor glass formation [12,13]. In addition, the dense packing within the 5-fold symmetry suggests a glass state that is brittle rather than ductile [14][15]. Previous studies also show crystal-like structure in metallic glass [16], which is mainly identified from 4-fold rotation symmetry. Crystal-like symmetry is thought to disfavor glass formation by promoting crystallization [17].

One way to measure local glass structure and rotational symmetry in amorphous materials is through electron nanodiffraction (END) [18]. An electron beam with the size of a few nanometers probes a set of atoms in a small sample volume. Structure information is encoded in the diffraction pattern, as local structures can give rise to Bragg-like coherent speckles [19]. The angular correlation function (ACF, defined below) is one way to extract rotational symmetries from these Bragg diffraction-like patterns. The ACF resolved in correlation angle and scattering wave vector is called a correlogram or correlograph. The ACF may also be Fourier transformed to obtain the angular power spectrum, in an effort to isolate particular

rotational symmetries. ACF analysis and correlograms have been used several times to study various glass structures. END experiments on amorphous silicon quantified paracrystallinity by fitting atomistic model against the average electron correlogram [20]. Local clusters in ZrNi metallic glass were modeled via simulation and END with a coherent nanoprobe with diameter less than 1 nanometer [21]. The spatial distribution of clusters or local structural symmetry was mapped by scanning the probe across the region of interest and acquiring a series of END patterns [22], a procedure now commonly called 4D STEM. ACF and angular power spectrum also have drawbacks, including lack of robustness against thicker samples [23][24]. Also, ENDs can lack Friedel symmetry, leading to challenges in interpretation [25]. Efforts have been made to refine angular correlation and power spectrum results in regard to these drawbacks. Liu *et al.* [26] calculated rotation averaged Fourier coefficients for several archetypical short-range clusters, which provides distinct fingerprints that can be used to identify preferred local arrangement. High quality, quantitative angular correlation analysis requires complex statistical analysis and theoretical modeling [27].

Here, we discuss several artifacts in the angular power spectrum of END patterns from amorphous materials that could be detrimental to determining structural symmetries: systematic ringing effects from Fourier transformation, chance correlations from random overlap of scatterers, and odd symmetries arising from nonstructural sources. Then, we introduce a new method for extracting structural symmetries from END data inspired by Symmetry-STEM, a novel method for extracting symmetry information from convergent beam electron diffraction (CBED) patterns in crystals [28]. Symmetry-STEM cross-correlates CBED patterns from a crystal structure with themselves after application of a symmetry operation. We use a similar approach to obtain correlation coefficients from which the symmetry coefficients are calculated to represent the magnitude of rotational symmetry in glass local structures. The new method avoids some but not all of the artifacts that affect the angular power spectrum. A simple mathematical model and END experiments on a Pd-Ni-Cu-P metallic glass illustrates the advantages of symmetry coefficient analysis over the angular power spectrum.

# 2. Methods

Figure 1a-c illustrate the process of angular correlation analysis. We start by calculating the ACF [29],

$$C(k,\Delta) = \frac{\langle I(k,\varphi)I(k,\varphi+\Delta)\rangle_{\varphi} - \langle I(k,\varphi)\rangle_{\varphi}^{2}}{\langle I(k,\varphi)\rangle_{\varphi}^{2}},$$
(1)

where  $\Delta$  is the correlation angle and  $I(k,\varphi)$  is the diffracted intensity in the END pattern in terms of scattering vector k and azimuthal angle  $\varphi$  defined in Fig.1a. Fig.1b shows the correlogram of the pattern in Fig 1a.  $C(k,\Delta)$  is then Fourier transformed to obtain the angular power spectrum,  $\hat{C}(k,n)$ , where n is the order of Fourier coefficient, shown in Fig.1c.  $\hat{C}(k,n)$  is power of the END pattern in polar coordinates. The Fourier amplitude for a particular (k,n) is interpreted as the magnitude of the rotational symmetry of the structure diffracted at that k.

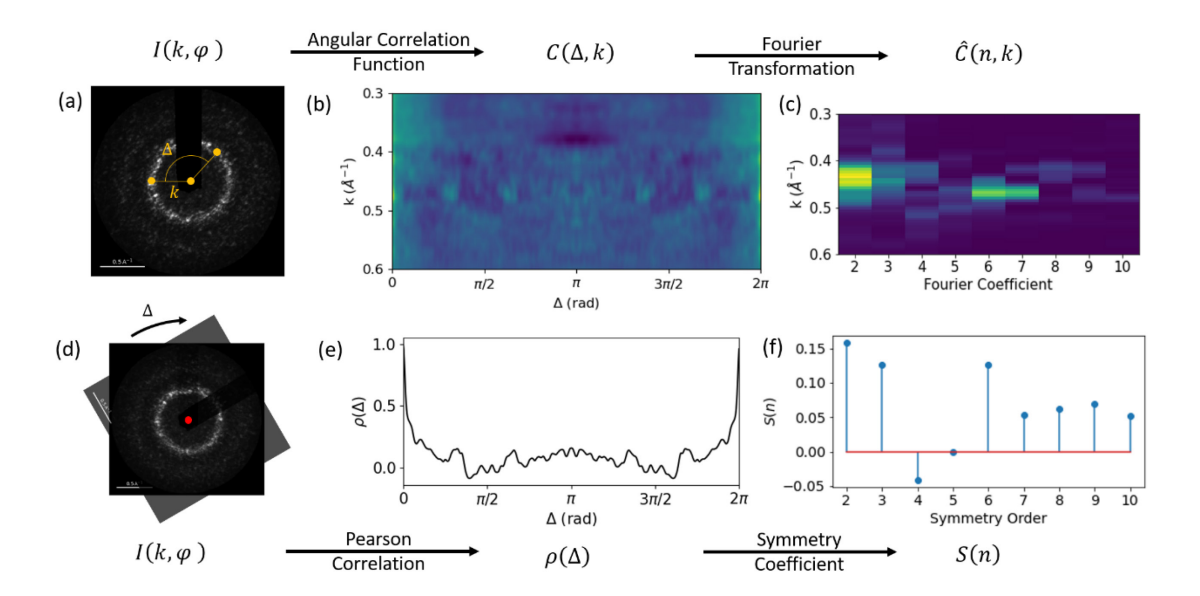


Figure 1. Schematics of angular correlation analysis and correlation symmetry analysis using an experimental END pattern on Pd-based nanowire sample. (a-c) Angular correlation analysis procedure; (d-f) Correlation symmetry analysis procedure

Figure 1d-f illustrates the process of correlation symmetry analysis, inspired by Symmetry-STEM [28]. We start by rotating the pattern around its origin as shown in Fig.1d. The Pearson product-moment correlation coefficient between the original and rotated patterns is calculated for different rotation angles  $\Delta$  as

$$\rho(\Delta) = \frac{\langle I(k,\varphi)I(k,\varphi+\Delta)\rangle_{k,\varphi} - \langle I(k,\varphi)\rangle_{k,\varphi}^2}{\langle I(k,\varphi)^2\rangle_{k,\varphi} - \langle I(k,\varphi)\rangle_{k,\varphi}^2}.$$
 (2)

Here,  $\langle ... \rangle_{k,\varphi}$  denotes average over wave vector k and azimuthal angle  $\varphi$ . If we average over all wave vectors, Eq.2 is the Pearson correlation of the whole pattern; if we average over a smaller k-range, Eq.2 becomes the Pearson correlation of a ring segment of the pattern. Theoretically,  $\rho(\Delta)$  could range from 1 to -1. In the example shown in Fig.1e,  $\rho(\Delta)$  fluctuates near zero at different rotation angles and approaches unity at small rotation angles. Symmetry-STEM for crystalline samples calculates the correlation coefficient for the entire pattern. As we will see in the discussion, averaging over a smaller k-range will improve signal quality for amorphous samples.

To assess rotational symmetry, Symmetry-STEM uses  $\rho(\Delta)$  at the rotation angle characteristic of the symmetry (e.g. 90° for four-fold symmetry). Sets of speckles in nanodiffraction patterns from amorphous materials are often fuzzy, incomplete, or simply missing some of the speckles that would complete the symmetry. Therefore, we evaluate the symmetry magnitude from  $\rho(\Delta)$  by calculating the symmetry coefficient S(n), shown in Fig.1f. The definition of symmetry coefficient for a given n follows two rules: (1) S(n) is the mean of  $\rho(\Delta)$  at the characteristic angles of n-fold rotation symmetry, excluding  $\Delta = 0$  and  $2\pi$ ; and (2) S(2n) does not sample the angles already included in S(n). The first few terms of S(n) are defined as

$$S(2) = \rho(\pi)$$

$$S(3) = [\rho(2\pi/3) + \rho(4\pi/3)]/2$$

$$S(4) = [\rho(\pi/2) + \rho(3\pi/2)]/2$$

$$S(5) = [\rho(2\pi/5) + \rho(4\pi/5) + \rho(6\pi/5) + \rho(8\pi/5)]/4$$

$$S(6) = [\rho(\pi/3) + \rho(5\pi/3)]/2$$
(3)

In this way, S(n) extracts symmetry information encoded at the characteristic rotation angles in the Pearson correlation  $\rho(\Delta)$ . We have investigated S(n) coefficients up to n = 10. We have implemented correlation symmetry analysis in open source pyXEM package for analysis of 4D STEM data [30].

Pd<sub>43</sub>Ni<sub>10</sub>Cu<sub>27</sub>P<sub>20</sub> nanowires with a diameter of ~40 nm were fabricated by nanomoulding as described in [31]. As-prepared nanowires were attached to a substrate plate of the same bulk metallic glass. The bulk metallic glass plate was rinsed with distilled water and isopropyl alcohol to minimize the residual salts and anodized aluminum oxide from fabrication. Then the plate was immersed in methanol solution and nanowires were released from the substrate by ultrasound for 15-20 min. The nanowires dispersed in methanol were dropped on to a DENSsolutions Wildfire TEM heating chip using a micropipette (1.5-1.8 μL). Nanowires were randomly attached to the 90% electron transparent SiN<sub>x</sub> membrane present on windows in the chip after methanol evaporated. 10-12 drops of the nanowire suspension in methanol were used, allowing 5 min methanol evaporation time between drops to achieve a uniform distribution of isolated nanowires. The sample was plasma cleaned for 10 mins in a 20 psi Ar + O2 mixture to remove organic contaminants before loaded into the microscope. END experiments were performed on an FEI Titan microscope at 200 kV acceleration voltage. A coherent probe 2.2 nm in diameter with 0.71 mrad semiconvergence angle was formed in microprobe mode. A camera length of 510 mm was used in energy filtered STEM mode with a 10 eV wide slit. The END patterns are acquired by a 2048×2048 Gatan CCD camera with binning factor of 4. The exposure time is set to 6 sec to ensure sufficient signal to noise ratio. The patterns are taken at an 8×20 grid of positions along the wire for multiple nanowires with sufficient spacing between each position to avoid overlap. A total of 960 patterns were recorded and used for the analysis.

#### 3. Results and Discussion

# 3.1 Limitations of the Angular Power Spectrum

ACF and the angular power spectrum suffer from three significant artifacts, all of which create symmetry signals that are not related to symmetries in the atomic structure. The first artifact originates from the familiar phenomena of ringing in the Fourier transform. In END experiments, the speckles are disks with a radius set by the convergence angle of the probe. The condenser aperture imposes a sharp angular cutoff, so the speckles also tend to have sharp edges. Sample scattering redistributes intensity within the speckle disks and causes some blurring of the sharp edges, but the basic disk shape remains.

To see the influence of the Fourier transform of the disk, consider an idealized diffraction pattern consisting of sharp-edged, flat disks with 2-fold Friedel symmetry as shown in Fig. 2a. The intensity of the pattern in azimuthal angle at wavevector  $k_c$  is

$$I_{k_{\mathcal{C}}}(\varphi) = \begin{cases} I_{0}, & 0 \le \theta \le w - 1, N/2 \le \theta \le N/2 + w - 1\\ 0, & \text{elsewhere} \end{cases}$$
 (4)

where  $k_c$  is the wavevector at the center of the disks,  $I_0$  is the intensity of the disk, N is the total number of discrete azimuthal angles and w is the width of the disk at  $k_c$  in azimuth. Without noise, the angular

intensity profile of an ideal 2-fold symmetrical END pattern at  $k_c$  is two identical rectangular functions  $\pi$  apart from each other, as shown in Fig. 2b. The ACF from Eq. 1 is a triangle wave, as shown in Fig. 2c, and the angular power spectrum is

$$\hat{C}_{k_c}(n) = \frac{\sin^2(\pi n w/N)}{\sin^2(\pi n/N)} (2 + 2\cos n\pi),\tag{5}$$

shown in Fig 2d. The term  $\sin^2(\pi nw/N) / \sin^2(\pi n/N)$  is a sinc function, the Fourier transform of the disk, and the term in parentheses is 0 for odd order and 1 for even order. As a result, the power spectrum of an ideal END with 2-fold rotational symmetry has power at all even orders as in Fig. 2d. The 2-fold power is smeared out to higher even orders because of the incompatibility between Fourier transformation, which uses sinusoids as the decomposition kernel, and the triangular ACF. An illustration of this ringing effect is shown in Fig.2c. The extent of first lobe in the sinc function is given by N/w. Therefore, as the probe convergence angle decreases, the ringing effect becomes more significant. END uses a fairly parallel beam, so this artifact can be significant.

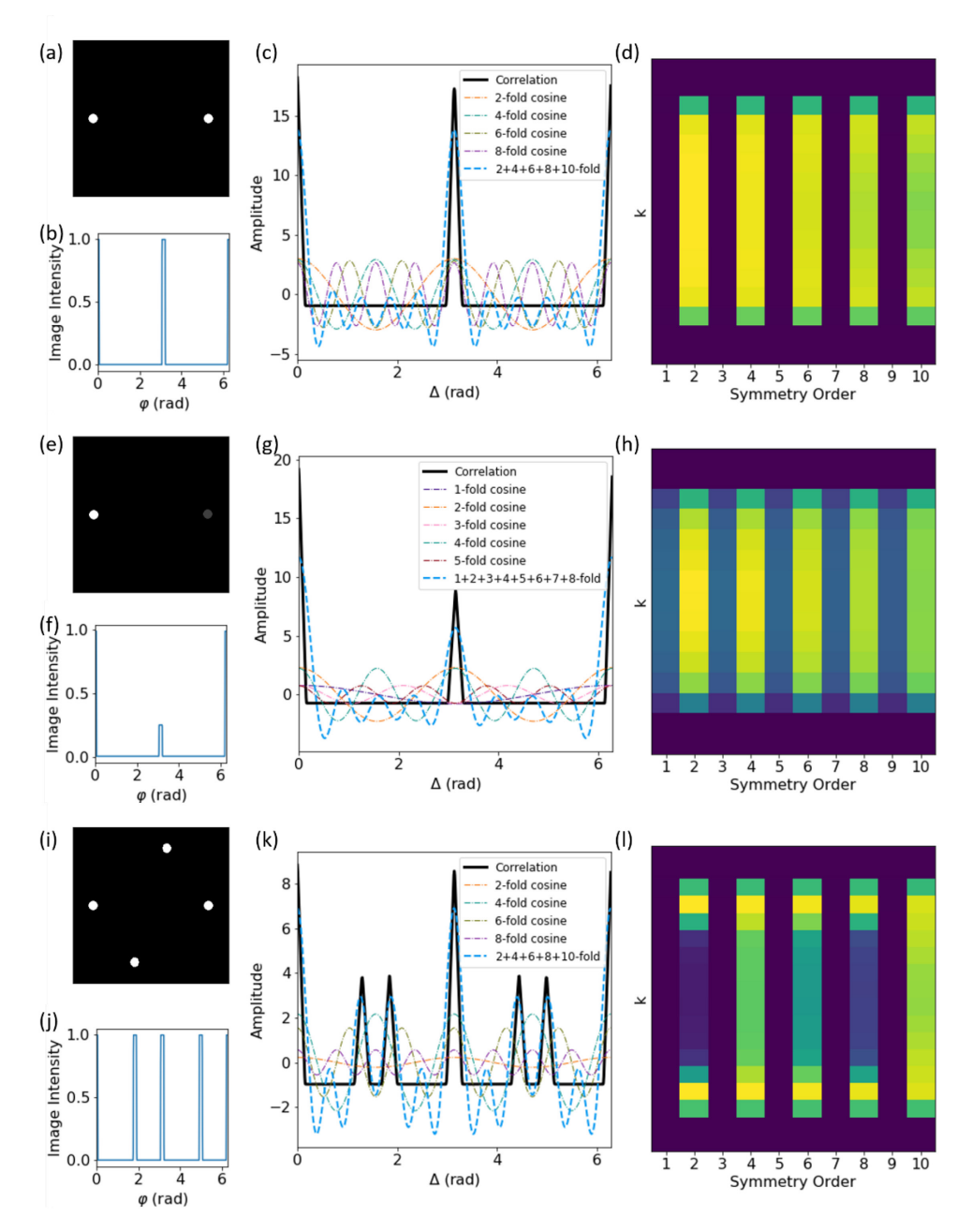


Figure 2. END patterns, azimuthal intensity profiles, angular correlation functions plotted with Fourier components, and angular power spectra of (a-d) ideal 2-fold crystallographic symmetry, (e-h) 2-fold crystallographic symmetry with broken Friedel symmetry, and (i-l) two randomly overlaid 2-fold crystallographic symmetries.

The second artifact arises from the breakdown of Friedel symmetry, which causes non-structural odd symmetry. If Friedel symmetry is maintained, i.e.  $I(k, \varphi) = I(k, \varphi + \pi)$ , the odd terms in angular power  $\hat{C}(k,n)$  vanish. The full three-dimensional reciprocal space of the sample is at least approximately centrosymmetric, and thin samples with nanometer-scale ordered diffracting clusters should result in very long relrods and Friedel symmetry in the diffraction pattern, no matter what orientation the diffracting object takes to the electron beam. However, Friedel symmetry is clearly violated in experimental patterns like Fig 1a. Friedel breakdown has been attributed to lens aberration and defocus [19,32], but the detailed

origins are not the primary concern here. In an END pattern without the Friedel symmetry, the odd terms in angular power are no longer zero. In the 2-fold crystallographic symmetry example, assuming one disk is p times stronger than its Friedel pair as shown in pattern Fig. 2e, the angular power becomes

$$\hat{C}_{k_c}(n) = \frac{\sin^2(\pi n w/N)}{\sin^2(\pi n/N)} (1 + p^2 + 2p \cos n\pi). \tag{6}$$

Now that the bracket term becomes non-zero for odd order, odd symmetries emerge in the angular power spectrum, as in Fig. 2h. The nature of these odd symmetry comes from the loss of  $C(\Delta = \pi)$  magnitude caused by the uneven speckle intensities. The odd sinusoid eigenfunctions need to be included to compensate for the loss. This effect can be misleading, as these odd symmetries are completely nonstructural. Real structural odd symmetries, like the 5-fold rotational symmetry of quasicrystals for example, diffract into even order that is twice the odd as per the Friedel law. In thick samples, Friedel symmetry breakdown can be significant. Im *et al.* have shown that the power spectrum for thick samples becomes a featureless band that monotonically decreases in n [24].

The third artifact arises from random overlap of multiple scatterers in the thickness of the sample, resulting in several superimposed sets of speckles. It is natural that multiple clusters can exist in the same sample column illuminated by electron probe. In this situation, if two or more of these clusters happened to be on or near a zone axis, their strong speckles will be overlaid in the pattern recorded at that probe position. An example of two randomly overlaid (randomly rotated in the diffraction plane) 2-fold crystallographic symmetry diffraction pairs with different k values is shown in Fig. 2i. The two pairs are about 70 degree apart from one another, which is close to the characteristic angles for 4- and 6-fold rotational symmetry. As a result, they give rise to artifact power in the n=4 and 6 symmetries at the k values they both share (Fig. 2j).

The simple mathematical model can be extended to treat all the three artifacts. Assume the pattern consists of m+1 pairs of diffraction disks with the same k value, with m of them rotated in  $\{\Delta_1, \Delta_2, ..., \Delta_m\}$  with regards to a reference pair. They have intensities of  $\{p_0, p'_0, p_1, p'_1, ..., p_m, p'_m\}$  where  $p_i$  and  $p_i$  are the intensities of the ith pair. The angular power of this pattern is given by

$$\hat{C}_{k_c}(n) = \frac{\sin^2(\pi n w/N)}{\sin^2(\pi n/N)} \left[ \sum_i (p_i \pm p_i')^2 + \sum_{i,j,i>j} 2(p_i \pm p_i')(p_j \pm p_j') \cos q(\Delta_i - \Delta_j) \right], \tag{7}$$

where  $q = 2\pi n/N$  and  $k_c$  is the wavevector at the center of the disks. Here, the  $\pm$  signs are + when n is even and - when n is odd. Eq. 7 shows that when Friedel symmetry breaks down  $(p_i - p_j \neq 0)$ , the diffraction disks and their corresponding Friedel pairs are only partially destructive at odd order, thus yielding non-zero odd power. The cosine term in Eq. 7 acts as a modulation between different diffraction pairs, which is the same modulation causing the false power in Fig. 2j.

In experimental data, the disks become speckles with more diffuse edges, which sit on a background of diffuse diffraction. Diffuse edges to the speckles smooth the correlation function in both k and  $\Delta$ . Smoothing in k leads to the widening of the band in the power spectrum, and smoothing in  $\Delta$  diminishes the high order power, leaving angular powers with physical meaning ( $n \le 10$ ) largely unaffected. Diffuse background does not have much influence on angular power, as it does not vary with angle very much. In addition, different structures or compositions of clusters have different atomic spacings and accordingly different k values. These limitations notwithstanding, Eq. 7 largely captures the behavior of angular power of END patterns, including the ringing effect from the sinc function, Friedel symmetry breakdown, and the

overlap of diffraction from different structures, all of which can make angular power spectrum results challenging to interpret.

### 3.2 Advantages of Correlation Symmetry Analysis

Correlation symmetry analysis diminishes or totally avoids the first two artifacts and may mitigate some effects of the third. Unlike the sinusoidal kernel for the angular power, correlation symmetry analysis uses  $\delta$  eigenfunctions (Fig. 3d), which are not subject to the systematic ringing artifacts. Fig. 3a shows the symmetry coefficient of the same diffraction pattern exhibited in Fig. 2a, and here only 2-fold symmetry magnitude is present. Nonstructural odd symmetry from Friedel symmetry breakdown will also not occur in the symmetry coefficients, as shown in Fig. 3b. Since in symmetry coefficient,  $S(2) = \rho(\pi)$ , the loss of magnitude in  $\rho(\Delta = \pi)$  causes a decrease in 2-fold  $\delta$  function (Fig. 3e) instead of any emergence of odd  $\delta$  functions. In correlation symmetry, 2-fold magnitude no longer serves as indicator for 2-fold rotational symmetry alone. It in fact represents all even rotational symmetries, *i.e.*, all ordering structures in the sample that give rise to strong Bragg-like speckles.

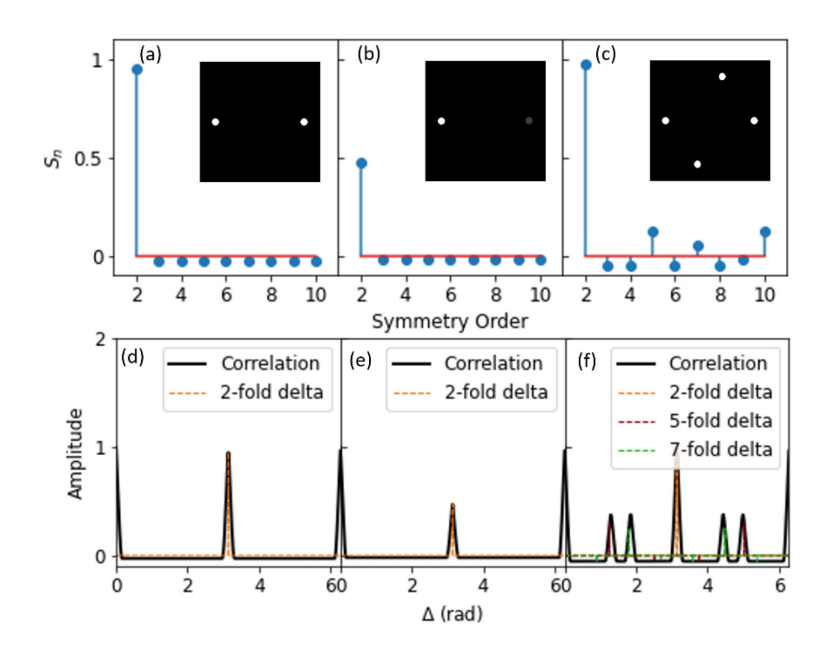


Figure 3 Symmetry coefficient profiles and Pearson correlation profiles plotted with  $\delta$  function kernels of (a, d) ideal 2-fold crystallographic symmetry, (b, e) 2-fold crystallographic symmetry with Friedel symmetry breakdown, and (c, f) two randomly overlaid 2-fold crystallographic symmetries. Inset images (a)-(c) are the corresponding END patterns.

Random overlap still plays a role in the symmetry coefficients, but the effect is reduced by the greater angular selectivity compared to the angular power. Since the symmetry coefficients defined in Eq. 3 only access the correlations at the exact angles of the rotational symmetries, correlations close to but not right at those angles will not be registered, which significantly reduces the probability of random overlap creating a high magnitude even symmetry. Fig. 3c shows the symmetry coefficient of the same random overlap pattern as in Fig. 2i. There is no false 4- and 6-fold symmetry coefficient, but there is some 5-, 7- and 10-fold symmetry coefficient. This is because in the formulations in Eq. 3, odd symmetries (and all high order symmetries for that matter) sample many more angles than low order even symmetries, which makes them

more likely to gain magnitude from random overlaps. However, odd symmetries arise from both inherent odd symmetries in the pattern as well as the even symmetries that are twice the odd (for instance, S(3) could come from both 3- and 6-fold symmetries).

#### 3.3 Application of Correlation Symmetry Analysis to Nanodiffraction Experiments

Fig. 4 compares angular power spectrum and symmetry analyses of 960 END patterns acquired from a moderately thick (41  $\pm$  3 nm) Pd<sub>43</sub>Ni<sub>10</sub>Cu<sub>27</sub>P<sub>20</sub> sample. Fig. 4a shows the pattern averaged angular power spectrum of the END data. The power decreases monotonically with increasing Fourier coefficient n in the k range of the first diffraction ring. This behavior is very similar to the power spectrum observed in the thick sample in [24]. Strong Friedel breakdown introduces high power in nonstructural odd symmetries, obscuring features in the spectrum that could be structurally significant. Fig. 4b shows the pattern averaged symmetry coefficients of the same data, averaged over the first diffraction ring segment (k = 0.4 to 0.5 Å <sup>1</sup>). Strong 10-fold symmetry is observed, as well as relatively significant 6-fold symmetry. 2-fold symmetry has the lowest magnitude, reflecting the breakdown of Friedel symmetry. The 4-fold symmetry coefficient is similar to the 3, 5, 7, and 9-fold odd symmetries. Past structural studies on Pd<sub>40</sub>Ni<sub>40-x</sub>Cu<sub>x</sub>P<sub>20</sub> metallic glass indicates that the preferred local atomic configuration is mixture of a Pd<sub>40</sub>Ni<sub>40</sub>P<sub>20</sub> type structure and a  $Pd_{40}Cu_{40}P_{20}$  type structure depending on the Cu composition [1,33]. The  $Pd_{40}Ni_{40}P_{20}$  type structure is mainly a P-centered tri-capped trigonal prisms (TTP), which contains near 6-fold and near 5-fold symmetry. High resolution TEM study also showed the possible existence of fcc-like clusters in Pd<sub>40</sub>Ni<sub>40</sub>P<sub>20</sub> [34]. The Pd<sub>40</sub>Cu<sub>40</sub>P<sub>20</sub> type structure is mainly a P-centered, transformed tetragonal dodecahedron which exhibits near 5-fold symmetry. The strong 10-fold symmetry in Fig. 4b is consistent with the near 5-fold structural symmetry in both structural types, and the 6-fold symmetry is consistent with the near 6-fold structural symmetry in Pd<sub>40</sub>Ni<sub>40</sub>P<sub>20</sub> type structure. The lack of strong 4-fold symmetry in the data suggests little or no fcc or other crystal-like structure in this glass.

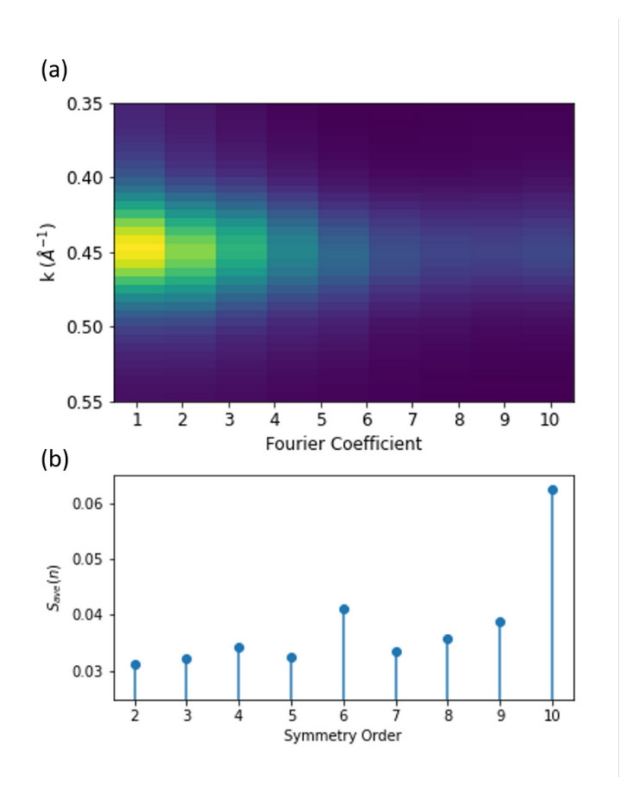


Figure 4 (a) Averaged power spectrum and (b) averaged symmetry coefficients of the END experiments on the Pd-based nanowires; (c, g) examples of END patterns, (d, h) their angular correlation functions at  $k = k_{\text{max}}$ , (e, i) power spectrum and (f, j) symmetry coefficients.

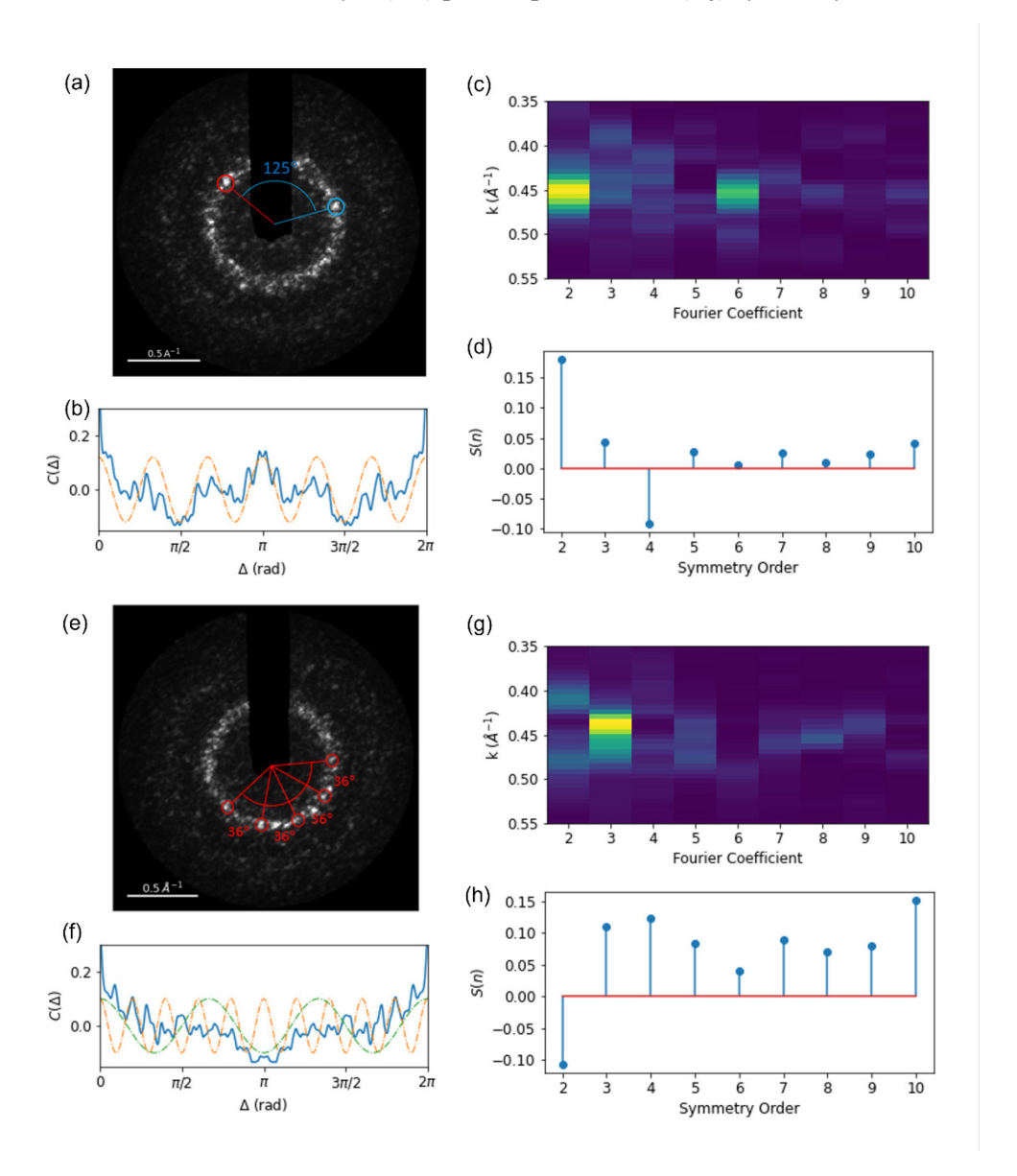


Figure 5 (a, e) Examples of END patterns, (b, f) their angular correlation functions at  $k = k_{\text{max}}$ , (c, g) power spectrum and (d, h) symmetry coefficients.

Fig. 5 compares power spectrum and symmetry analyses of illustrative individual patterns, along with a slice of the angular correlation function at selected k. In the END pattern shown in Fig. 5a, two strong speckles form at an angle of  $\sim 125$  degrees, which is not associated with a symmetry with n < 10. Fig. 5b shows the  $C(\Delta)$  profile of that pattern at k = 0.45 Å<sup>-1</sup>, with a 6-fold Fourier kernel overlay on the plot. The correlation profile has peaks near but not exactly aligned with  $\Delta = n\pi/3$ , a result of the near 120 degree correlation. The power spectrum reflects this as a false "6-fold" symmetry as shown in Fig. 5c, but symmetry coefficient in Fig. 5d does not indicate any strong 6-fold symmetry. In the END pattern shown in Fig. 5e, there is a set of five speckles 36 degrees apart from each neighboring one, which is the angle for

10-fold symmetry, so these speckles represent significant 10-fold symmetry that is only partially complete in the diffraction plane of the camera. The correlation profile  $C(\Delta)$  at k=0.45 Å<sup>-1</sup> in Fig. 5f is overlaid with 3-fold and 10-fold Fourier kernels. The correlations among the speckles inside the set of five give rise to the peak in  $C(k, \Delta)$  at  $\Delta = \pi/5$  as well as two smaller peaks at  $\Delta = 3\pi/5$  and  $4\pi/5$ . While these peaks fit the 10-fold characteristic angles very well, 10-fold symmetry is not recognized in the power spectrum, as the pattern is incomplete. Even though there are no peaks at the 3-fold rotational symmetry positions, since there are other strongly diffracted speckles in this pattern, the power spectrum is heavily modulated by them and thus falsely identifies a 3-fold symmetry in Fig. 5g. On the other hand, the symmetry coefficient shown in Fig. 5h registers the angles marked in Fig. 5e, generating a strong 10-fold symmetry magnitude. These two patterns experimentally demonstrate the instability of power spectrum analysis to non-structural random overlap correlations and Friedel symmetry breakdown artifacts. Correlation symmetry analysis has lower sensitivity to the same artifacts when applied to the same data.

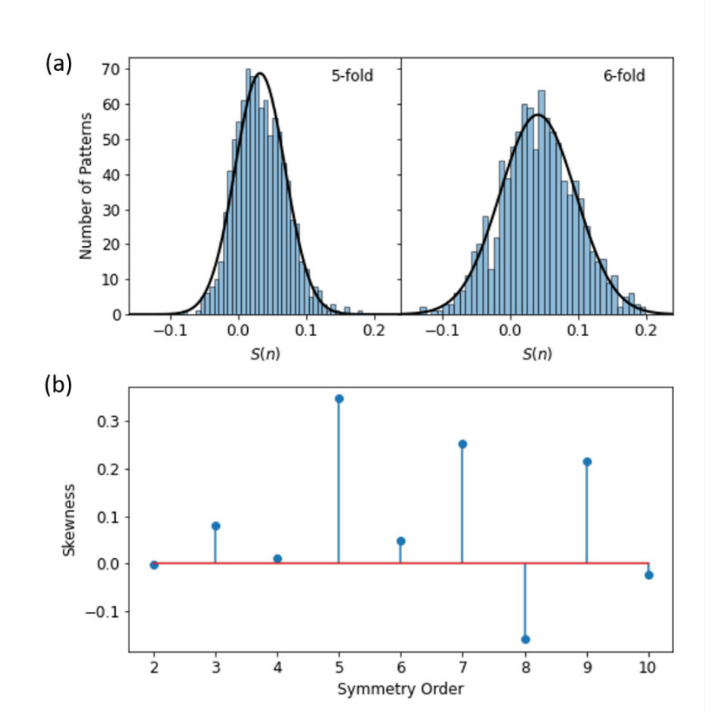


Figure 6 (a) Symmetry coefficient distributions S(n) for 5- and 6-fold symmetry. Solid lines are Gaussian fit of the distributions; (b) Skewness of the distributions of symmetry coefficients S(n).

It is tempting to interpret even symmetry coefficients as arising from symmetries in the structure and odd coefficients as arising from artifacts. In Fig. 4b, the odd and even symmetry coefficients are comparable, except for n = 10. Does that mean that all of the other symmetry coefficient signals are non-structural? 3- and 5-fold symmetry can have some contribution from structural, Friedel-symmetric 6- and 10-fold symmetries in the END patterns, but 7- and 9-fold symmetries in the pattern should occur only from random overlaps. Constructing a general model to separate structural from non-structural symmetries is a substantial challenge, but a preliminary statistical analysis of the symmetry coefficient distributions suggests that it might be possible. Fig. 6a compares the symmetry coefficient distributions for n = 5 and n = 6. The n = 6 distribution is nearly Gaussian, but the n = 5 distribution is skewed towards the left and has a tail on the righthand side. It may even be bimodal, although current data is insufficient to test this hypothesis. Fig. 6b

shows the skewness of the symmetry coefficient distribution for n = 2 to 10, which is sensitive to asymmetry in the distribution. The even symmetries have near zero skewness (except for 8-fold symmetry) whereas the odd symmetries have relatively high positive skewness. This means for the odd symmetries, the distributions are skewed to the left side and has a long tail to the right. One possible origin for this behavior is a main distribution with a mean of low S(n) values and a few outliers from the random overlaps with much higher S(n). For even symmetries, the distributions are more symmetric around the mean, indicating a higher probability of having a structure-related monomodal distribution. However, this interpretation is not consistent with the negative skewness for the 8-fold distribution, which is not an allowed crystallographic symmetry, so clearly more work is needed.

Fig. 7 compares the Pearson correlation  $\rho(\Delta)$  profiles of the END pattern in Fig. 1a integrated over the whole pattern and integrated only over the first diffraction ring (k = 0.4 to  $0.5 \text{ Å}^{-1}$ ). They possess similar features, but integrating over the k range of the first diffraction ring generates higher signal to background ratio. This is probably due to the diffuse diffraction background and random noise, both of which play more significant roles at higher k as the speckle intensity drops. It also suggests the possibility of achieving moderate k-resolution in correlation symmetry analysis by integrating in ring segments of different k. Such an approach might, for example, separate the influence of structures in the sample diffract at differing k due to differing local compositions and interatomic spacings.

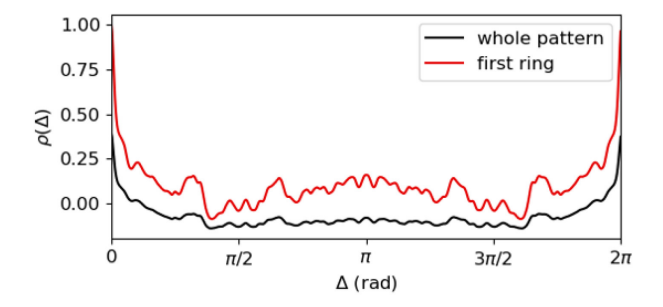


Figure 7 Pearson correlation  $\rho(\Delta)$  of the END pattern in Fig.1a by integrating the whole pattern (black) and only the first diffraction ring (k = 0.4 to  $0.5 \text{ Å}^{-1}$ ) (red).

The END patterns analyzed here were acquired with a CCD detector and fairly long acquisition time. Densely-spaced fast 4D STEM acquisition of END data with high speed camera can map local clusters in a sample [35]. With symmetry coefficient data at each of the probe positions, machine learning approaches like multidimensional clustering could be utilized to identify the symmetry, size, and relative position of individual clusters. Correlation symmetry analysis could also have potential applications in semicrystalline polymers [36], amorphous silicon [20], anisotropically ordered molecular glasses [2], and other systems.

#### 4. Conclusion

Angular power spectrum analysis of rotational symmetries in electron nanodiffraction patterns of amorphous materials is prone to systematic and experimental artifacts. The Fourier transformation of the sharp-edged speckles in the pattern produces contributions to higher-order power from lower-order physical symmetries, Friedel symmetry breakdown in the pattern creates non-structural odd order power, and speckles in random orientations created by diffraction from different ordered clusters within the same column of the material sampled by the probe create power which does not reflect structural symmetries. Correlation symmetry analysis avoids or mitigates all of these artifacts. It avoids ringing artifacts by avoiding Fourier transformation, and by probing only specific angles, it decreases the effects of Friedel symmetry breaking and chance arrangements of speckles from different ordered clusters. Correlation

symmetry analysis applied to a  $Pd_{43}Ni_{10}Cu_{27}P_{20}$  sample confirms the presence of 6- and 10-fold rotational symmetries in the sample, indicating the existence of both  $Pd_{40}Ni_{40}P_{20}$  and  $Pd_{40}Cu_{40}P_{20}$  type structures. Higher speed 4D STEM experiments with correlation symmetry analysis should be able to map more reliably local rotational symmetries in amorphous materials.

## Acknowledgements

This research was supported by the US National Science Foundation (DMR-1807241). Experimental data were collected using facilities supported by the Wisconsin Materials Research Science and Engineering Center (DMR-1720415).

# **Data Availability**

The datasets generated and analyzed in this work are available at [37].

#### Reference

- [1] Y.Q. Cheng, E. Ma, Atomic-level structure and structure-property relationship in metallic glasses, Prog. Mater. Sci. 56 (2011) 379–473. https://doi.org/10.1016/j.pmatsci.2010.12.002.
- [2] A. Gujral, L. Yu, M.D. Ediger, Anisotropic organic glasses, Curr. Opin. Solid State Mater. Sci. 22 (2018) 49–57. https://doi.org/10.1016/j.cossms.2017.11.001.
- [3] G. Calas, L. Cormier, L. Galoisy, P. Jollivet, Structure–property relationships in multicomponent oxide glasses, Comptes Rendus Chim. 5 (2002) 831–843. https://doi.org/https://doi.org/10.1016/S1631-0748(02)01459-5.
- [4] J.D. Bernal, A geometrical approach to the structure Of liquids, Nature. 183 (1959) 141–147. https://doi.org/10.1038/183141a0.
- [5] W. Zachariasen, The atomic arrangement in glass, J. Am. Chem. Soc. 54 (1932) 3841–3851. https://doi.org/10.1021/ja01349a006.
- [6] E. Ma, Tuning order in disorder, Nat. Mater. 14 (2015) 547–552. https://doi.org/10.1038/nmat4300.
- [7] F.C. Frank, J.S. Kasper, Complex alloy structures regarded as sphere packings. I. Definitions and basic principles, Acta Crystallogr. 11 (1958) 184–190. https://doi.org/10.1107/S0365110X58000487.
- [8] F.C. Frank, J.S. Kasper, Complex alloy structures regarded as sphere packings. II. Analysis and classification of representative structures, Acta Crystallogr. 12 (1959) 483–499. https://doi.org/10.1107/S0365110X59001499.
- [9] M.M.J. Treacy, P.M. Voyles, J.M. Gibson, Schläfli cluster topological analysis of medium range order in paracrystalline amorphous semiconductor models, J. Non. Cryst. Solids. 266–269 (2000) 150–155. https://doi.org/10.1016/S0022-3093(99)00794-2.
- [10] H.W. Sheng, W.K. Luo, F.M. Alamgir, J.M. Bai, E. Ma, Atomic packing and short-to-medium-range order in metallic glasses., Nature. 439 (2006) 419–25. https://doi.org/10.1038/nature04421.
- [11] D.R. Nelson, F. Spaepen, Polytetrahedral Order in Condensed Matter, in: H. Ehrenreich, D.B.T.-S.S.P. Turnbull (Eds.), Supercond. Quasicrystals Two Dimens. Phys., Academic Press, 1989: pp. 1–90. https://doi.org/10.1016/S0081-1947(08)60079-X.

- [12] Y.Q. Cheng, E. Ma, H.W. Sheng, Atomic level structure in multicomponent bulk metallic glass, Phys. Rev. Lett. 102 (2009) 1–4. https://doi.org/10.1103/PhysRevLett.102.245501.
- [13] N. Jakse, A. Pasturel, Glass forming ability and short-range order in a binary bulk metallic glass by ab initio molecular dynamics, Appl. Phys. Lett. 93 (2008) 113104. https://doi.org/10.1063/1.2976428.
- [14] H.L. Peng, M.Z. Li, W.H. Wang, Structural Signature of Plastic Deformation in Metallic Glasses, Phys. Rev. Lett. 106 (2011) 135503. https://doi.org/10.1103/PhysRevLett.106.135503.
- [15] J. Ketkaew, W. Chen, H. Wang, A. Datye, M. Fan, G. Pereira, U.D. Schwarz, Z. Liu, R. Yamada, W. Dmowski, M.D. Shattuck, C.S. O'Hern, T. Egami, E. Bouchbinder, J. Schroers, Mechanical glass transition revealed by the fracture toughness of metallic glasses, Nat. Commun. 9 (2018) 1–7. https://doi.org/10.1038/s41467-018-05682-8.
- [16] D.B. Miracle, A structural model for metallic glasses., Nat. Mater. 3 (2004) 697–702. https://doi.org/10.1038/nmat1219.
- [17] P. Zhang, J.J. Maldonis, M.F. Besser, M.J. Kramer, P.M. Voyles, Medium-range structure and glass forming ability in Zr-Cu-Al bulk metallic glasses, Acta Mater. 109 (2016) 103–114. https://doi.org/10.1016/j.actamat.2016.02.006.
- [18] J.M. Cowley, Electron nanodiffraction methods for measuring medium-range order, Ultramicroscopy. 90 (2002) 197–206. https://doi.org/10.1016/S0304-3991(01)00130-9.
- [19] J.M. Rodenburg, Properties of electron microdiffraction patterns from amorphous materials, Ultramicroscopy. 25 (1988) 329–343. https://doi.org/https://doi.org/10.1016/0304-3991(88)90007-1.
- [20] J.M. Gibson, M.M.J. Treacy, T. Sun, N.J. Zaluzec, Substantial crystalline topology in amorphous silicon, Phys. Rev. Lett. 105 (2010) 1–4. https://doi.org/10.1103/PhysRevLett.105.125504.
- [21] A. Hirata, P. Guan, T. Fujita, Y. Hirotsu, A. Inoue, A.R. Yavari, T. Sakurai, M. Chen, Direct observation of local atomic order in a metallic glass, Nat. Mater. 10 (2011) 28–33. https://doi.org/10.1038/nmat2897.
- [22] A.C.Y. Liu, M.J. Neish, G. Stokol, G.A. Buckley, L.A. Smillie, M.D. De Jonge, R.T. Ott, M.J. Kramer, L. Bourgeois, Systematic mapping of icosahedral short-range order in a melt-spun Zr 36Cu64 metallic glass, Phys. Rev. Lett. 110 (2013) 1–5. https://doi.org/10.1103/PhysRevLett.110.205505.
- [23] T. Sun, M.M.J. Treacy, T. Li, N.J. Zaluzec, J.M. Gibson, The importance of averaging to interpret electron correlographs of disordered materials, Microsc. Microanal. 20 (2014) 627–634. https://doi.org/10.1017/S1431927613014116.
- [24] S. Im, Z. Chen, J.M. Johnson, P. Zhao, G.H. Yoo, E.S. Park, Y. Wang, D.A. Muller, J. Hwang, Direct determination of structural heterogeneity in metallic glasses using four-dimensional scanning transmission electron microscopy, Ultramicroscopy. 195 (2018) 189–193. https://doi.org/10.1016/j.ultramic.2018.09.005.
- [25] A.C.Y. Liu, G.R. Lumpkin, T.C. Petersen, J. Etheridge, L. Bourgeois, Interpretation of angular symmetries in electron nanodiffraction patterns from thin amorphous specimens, Acta Crystallogr. Sect. A Found. Adv. 71 (2015) 473–482. https://doi.org/10.1107/S2053273315011845.
- [26] A.C.Y. Liu, R.F. Tabor, L. Bourgeois, M.D. De Jonge, S.T. Mudie, T.C. Petersen, Calculation of Projected Bond-Orientational Order Parameters to Quantify Local Symmetries from Transmission

- Diffraction Data, Phys. Rev. Lett. 116 (2016) 1–5. https://doi.org/10.1103/PhysRevLett.116.205501.
- [27] E. Bojesen, T.C. Petersen, A. Martin, M. Weyland, A. Liu, Statistical measures of angular correlations in amorphous materials from electron nano-diffraction in the scanning/transmission electron microscope, J. Phys. Mater. (2020) 11–14. https://doi.org/10.1088/2515-7639/aba820.
- [28] M. Krajnak, J. Etheridge, A symmetry-derived mechanism for atomic resolution imaging, Proc. Natl. Acad. Sci. U. S. A. 117 (2020) 27805–27810. https://doi.org/10.1073/pnas.2006975117.
- [29] P. Wochner, C. Gutt, T. Autenrieth, T. Demmer, V. Bugaev, A.D. Ortiz, A. Duri, F. Zontone, G. Grübel, H. Dosch, X-ray cross correlation analysis uncovers hidden local symmetries in disordered matter, Proc. Natl. Acad. Sci. 106 (2009) 11511 LP 11514. https://doi.org/10.1073/pnas.0905337106.
- [30] D.N. Johnstone, P. Crout, M. Nord, J. Laulainen, S. Høgås, EirikOpheim, B. Martineau, C. Francis, T. Bergh, E. Prestat, S. Smeets, andrew-ross1, S. Collins, I. Hjorth, Mohsen, T. Furnival, D. Jannis, N. Cautaerts, E. Jacobsen, AndrewHerzing, T. Poon, H.W. Ånes, J. Morzy, S. Huang, phillipcrout, T. Doherty, affaniqbal, T. Ostasevicius, mvonlany, R. Tovey, pyxem/pyxem: pyxem 0.13.2, (2021). https://doi.org/10.5281/ZENODO.4687011.
- [31] G. Kumar, H.X. Tang, J. Schroers, Nanomoulding with amorphous metals., Nature. 457 (2009) 868–72. https://doi.org/10.1038/nature07718.
- [32] M. Hytch, J. Chevalier, On the breakdown of Friedel's Law for coherent microdiffraction from amorphous materials, Ultramicroscopy. 58 (1995) 114–121. https://doi.org/10.1016/0304-3991(94)00184-O.
- [33] C. Park, M. Saito, Y. Waseda, N. Nishiyama, A. Inoue, Structural Study of Pd-Based Amorphous Alloys with Wide Supercooled Liquid Region by Anomalous X-ray Scattering, Mater. Trans. JIM. 40 (1999) 491–497. https://doi.org/10.2320/matertrans1989.40.491.
- [34] A. Hirata, Y. Hirotsu, T. Ohkubo, N. Tanaka, T.G. Nieh, Local atomic structure of Pd-Ni-P bulk metallic glass examined by high-resolution electron microscopy and electron diffraction, Intermetallics. 14 (2006) 903–907. https://doi.org/10.1016/j.intermet.2006.01.007.
- [35] C. Ophus, Four-Dimensional Scanning Transmission Electron Microscopy (4D-STEM): From Scanning Nanodiffraction to Ptychography and Beyond, Microsc. Microanal. (2019) 563–582. https://doi.org/10.1017/S1431927619000497.
- [36] O. Panova, X.C. Chen, K.C. Bustillo, C. Ophus, M.P. Bhatt, N. Balsara, A.M. Minor, Orientation mapping of semicrystalline polymers using scanning electron nanobeam diffraction, Micron. 88 (2016) 30–36. https://doi.org/https://doi.org/10.1016/j.micron.2016.05.008.
- [37] [dataset] S. Huang, C. Francis, J. Ketkaew, J. Schroers, P.M. Voyles, Data for Correlation Symmetry Analysis of Electron Nanodiffraction from Amorphous Materials, Mater. Data Facil. (2021). https://doi.org/10.18126/Y6L9-TS2N.